Platinum electrochemistry through a magnifying glass

Jacobse, L.

Citation

Jacobse, L. (2018, November 29). *Platinum electrochemistry through a magnifying glass*. Retrieved from https://hdl.handle.net/1887/67104

Author: Jacobse, L.
Title: Platinum electrochemistry through a magnifying glass
Issue Date: 2018-11-29

C Surface site identification of roughened Pt(111)

C.1 Average nanoisland

Determination of the average atomic island growth shapes starts from the drift-corrected EC-STM images as described in Appendix A. Subsequently, we have to; identify the individual islands and their boundaries; correct the height offset of the image (due to background subtraction); calculate the average measured island; and finally fit an fcc lattice to these average shapes. In the following, we describe the various steps in detail. Figure C.1 visualizes the overal process.

The initial island identification is performed using the built-in treshold and watershed functions in the GWYDDION SPM software.[1] A combination of Laplace filtering and constructing Voronoi cells is used to determine the island boundaries, see Fig C.1A. At this point, we filter out features that were identified as islands, but which are most likely tip effects, see the turquoise islands in Fig. C.1A. Not only are these islands significantly smaller, but in the STM images they are also poorly resolved, indicating tunneling via a double tip. The existence of these small islands leads to a bimodal island 'footprint' distribution. We can easily filter them out by applying a treshold to this distribution. For the averaging process, we find that the position of the absolute maximum within an island boundary yields slightly more accurate center positions compared to those found by the GWYDDION watershed function: we find that it leads to sharper average island shapes. The difference in center locations between these two methods is comparable to the size of the data points in Fig. C.1A. The entire surface is lifted with the absolute minimum of the considered surface area, in order to prevent averaging artifacts based on negative values. Finally, the average island is calculated via:

$$H(\mathbf{r}) = \frac{\sum_{n=1}^{n=n_{max}} h_n(\mathbf{r} - r_{0,n})}{n_{max}}, \tag{C.1}$$

where $H(\mathbf{r})$ is the average island, h_n is the n^{th} island, centered around $(r_{0,n})$, and n_{max} is the total number of analysed islands. An example of the averaging procedure is shown in Fig. C.1B.

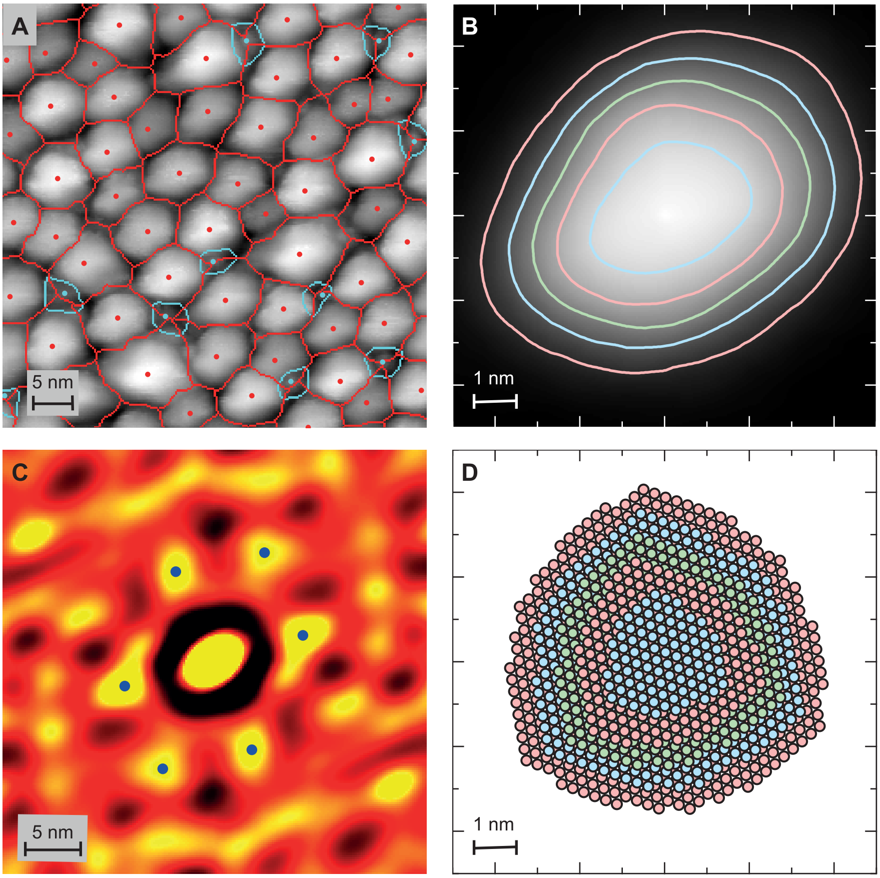

Fig. C.1 | Nanoisland averaging and structure determinations: (A) part of a background-corrected EC-STM image (after 110 ORCs) indicating the island centers and their boundaries. The turquoise dots and lines indicate islands that are considered to be tip effects, the red data is the final input for the averaging procedure. **(B)** Averaged nanoisland. The contour lines indicate heights of integer monolayers within this averaged island. **(C)** Result of a 2D autocorrelation analysis of the background-corrected EC-STM image shown in (A). The first order maxima (indicated by the dark blue markers) from all images are used to determine the lattice orientation. **(D)** The fitting result. The colors of the different atomic layers are the same as those of the contour plot in (B).

C.2 Structural fits

Both 2D autocorrelation functions and height-difference correlation functions of the different STM images resemble a (distorted) hexagonal pattern, as expected from the Pt(111) symmetry. This is exemplified in Fig. C.1C. To reduce the number of fitting variables, the (distorted) hexagonal structure was used to fix the rotation of the fcc lattice in the fitting process. In principle, however, this approach does not provide means to distinguish between the {100} and {111} direction. Nonetheless, as the islands are only slightly asymmetric and the steps at the {100}-side 'roughen', this does not significantly hamper our analysis.

Any STM experiment always suffers from convolution between the surface features and the shape of the STM tip. If the shape of the tip is known, one can correct the images to some extent.[2] Such deconvolution calculations consist of the erosion of the STM image ($A(\mathbf{r})$) by a so-called structure element ($b(\mathbf{r})$) that describes the tip geometry:

$$A_{deconvoluted}(\mathbf{r}) = (A \ominus b)(\mathbf{r}) = \min_{\mathbf{s}\in B}[A(\mathbf{r}+\mathbf{s}) - b(\mathbf{s})], \qquad \text{(C.2)}$$

where min indicates the minimum, B is the space in which $b(\mathbf{r})$ is defined.[3] A typical tip can be described as a cone ending in a spherical apex. Deconvolution calculations, illustrated in Fig. C.2, indicate that our tip has a tip radius of about 1.5 nm. For larger radii, imaging artefacts clearly start to appear, as can be seen from the changing island shape and the thin lines that run in between the islands. This effect, most dramatically observed in Fig. C.2F, implies an overestimation of the convolution. On top of this, however, the asymmetry in the average island (Fig. C.1B) indicates that the tip used in this experiment does have a significant radial asymmetry. From repeated, similar experiments with other tips, of which some data are shown in Fig. C.3, we conclude that this asymmetry is indeed a tip effect and that the formed islands exhibit the expected threefold symmetry. If one would intend to correct the data for both the tip asymmetry and size (without additional tip characterization), the asymmetry would have to be removed first to prevent artefacts due to overestimation of the tip radius. However, implementing this in an analytical routine is far from trivial. The asymmetry seems to have the largest influence on our analysis, which is why we employ a threefold island symmetry as boundary condition in the fitting procedure to correct for it. As any tip size/shape will always lead to an overestimation of the island shape, we argue that the minimum height in all directions of the threefold symmetry describes the real island shape most accurately. This approach also minimizes the general tip convolution effect, but no additional corrections are applied to further reduce this.

With the threefold minimum as boundary condition, and using the offset in the x- and y-direction as fit parameters, we consider the island structure for which the number of atoms underneath the average island contour is largest to be the best fitting result. We choose this approach because it is much more likely that an STM measurement overestimates the actual surface height (e.g. due to adatom/adsorbate diffusion or tip convolution), than that it underestimates the surface height. In the case that multiple structures occur which contain the same (maximum) number of atoms, the island structure that leads to the smallest fitting error (chi-square) with respect to the average island contour is preferred.

C.3 Site densities

To fully capture the electrochemical reactivity in the site densities, it is necessary to take into account the spacing between step edges in the different layers. Thus, in the three relevant directions, we distinguish step sites and various facet sites: ‘wide facets’, ‘narrow facets’, and ‘low index facets’. We label the islands sides according to the geometry of the corresponding step sites, i.e. {100}-, {110}-, and {112}-side (‘100% kinked’). In principle the {110} step edge can also be described as {111} step edge. However, this assignment would complicate describing the full surface due to the shape of the {111} step unit cell. Also, the description from a {110} step edge makes the facet assignment intuitively better comparable to that of the {100} step edge. Figure C.4 gives an overview of the different unit cells used for counting these site densities; Table C.1 gives the corresponding site description. The most intuitive way to understand the site assignment, is by looking at the terrace sites adjacent to the actual ‘defect’ site. Note that, instead a trapezoidal unit cell, we use small triangular sites for this description (*vide infra*). Looking at how these triangular terrace sites are surrounded by sites belonging to a ‘defect’ in a different atomic layer, we distinguish four different possibilities: (1) the terrace sites are completely separated from each other, these are ‘separated defects’; (2) the terrace sites are touching, the ‘defects’ are still considered to be separated (e.g. step sites are still counted as steps and not yet as facets), but the terrace sites are now listed as ‘wide facets’; (3) the terrace sites have adjacent sites, both ‘defect’ and terrace sites are now counted as ‘narrow facets’; (4) terrace sites are overlapping or completely missing, these are the ‘low index facets’. This assignment is slightly complicated for corner sites, which is why ‘wide facets’ are not used for

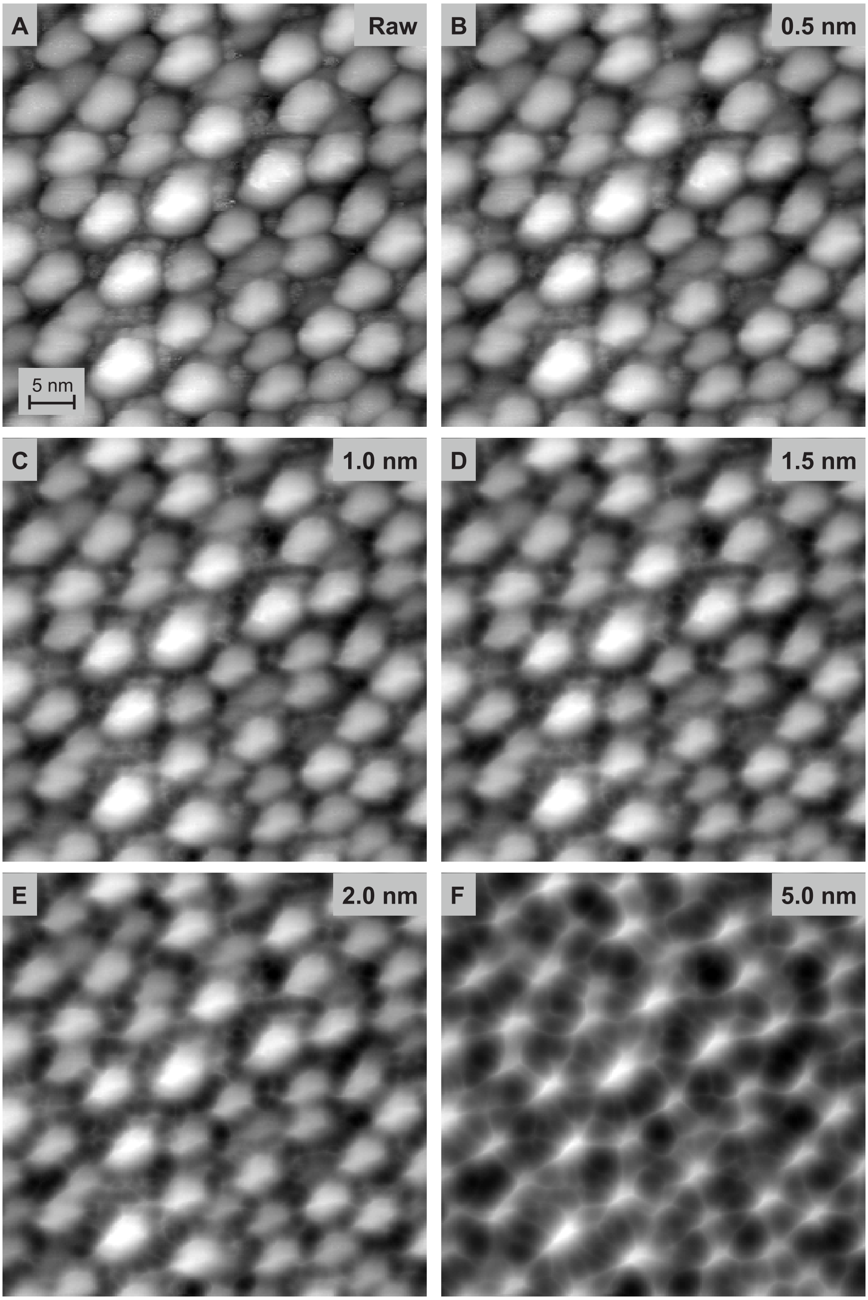

Fig. C.2 | Tip deconvolution results: **(A)** Part of an original EC-STM image. **(B)-(F)** The same data after applying the erosion operation[2] using tip radii of 0.5, 1.0, 1.5, 2.0, and 5.0 nm, respectively. The opening angle of the cone is fixed at 60°. The color scale is the same in all images. Note the sharp features and lines between the islands that appear for tips larger than 1.5 nm. As they are smaller than one atom, the tip radius is too large.

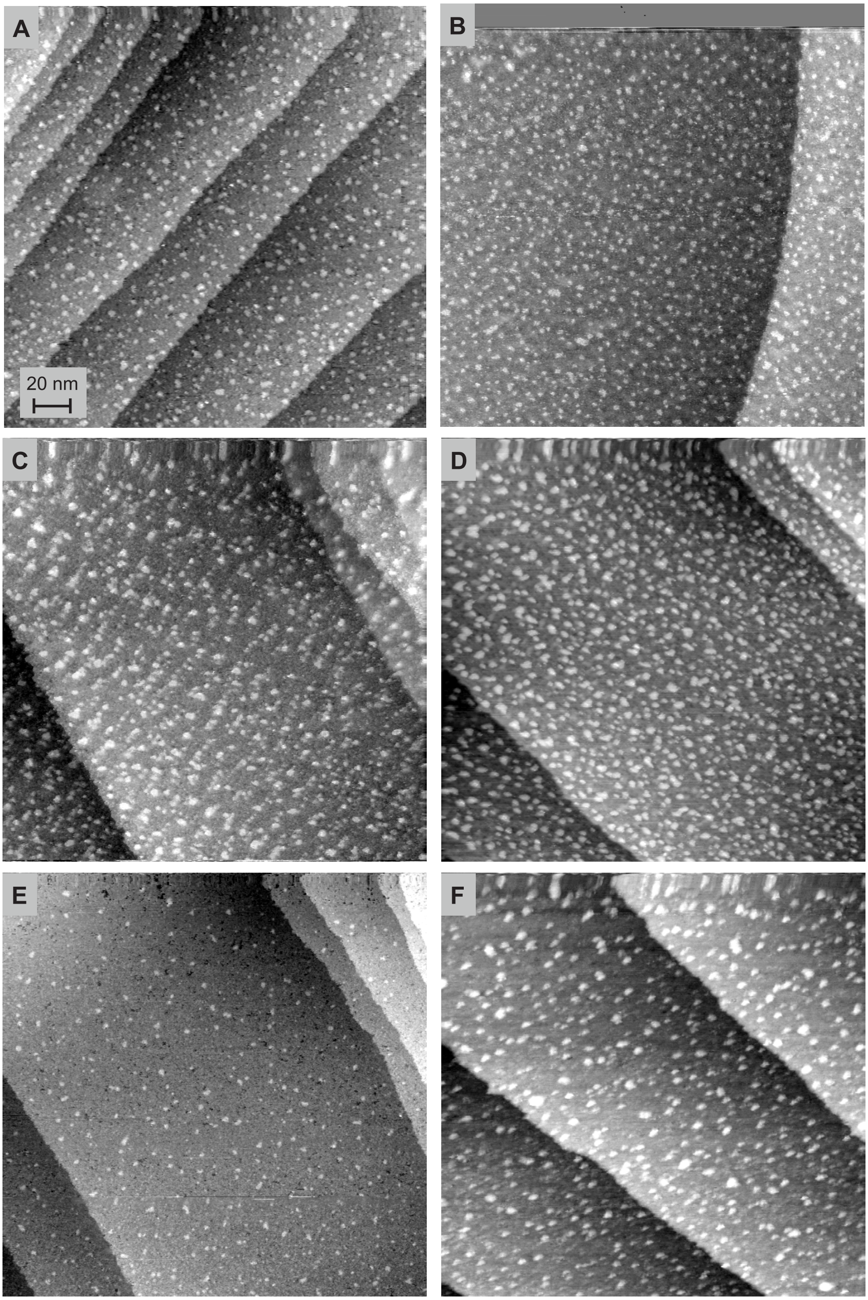

Fig. C.3 | Island shape comparison: EC-STM images from different experiments after some potential cycles. The images show neither that the islands do have a clear asymmetry in shape nor that the direction of the step edge influences the island asymmetry. This supports the argument that the observed asymmetry (clearest in Fig. C.1B) originates from a tip effect. All images are approximately 230x230 nm^2.

corners. Instead, if the terrace site contains one and/or two undercoordinated atoms, both the terrace and the corner itself are counted as ‘narrow facets’. If the terrace site is missing, the corner forms a ‘low index facet’. Note that at the {111}- and {112}-side, we could increase the surface slope even further by forming {111}-facets and {210}-facets, respectively. However, such sites are not observed in the average island structure. Table C.1 also mentions the formation of {211} and {221} kink facets, which are not shown in Fig. C.4. Such sites occur on a step edge that forms a ‘narrow facet’ (green), when one of the kink sites is translated one atomic distance along the step edge.

To be able to assign all sites on the surface, it is sometimes necessary to use sites that are smaller than whole unit cells. To determine the correct site densities,one must therefore apply the appropriate prefactors: two triangular terrace sites form one full terrace site; steps, facets, and kinks in the {100} and {111} direction consist of two times $^1/_2$ site; the steps/facets in the {112} direction of two times 1 site; and corner sites count as $^1/_2$ site. Table C.2 gives the counts of the different sites as indicated by the colored planes in Fig. C.4. Figure SC.5 shows all the individual site densities as counted from the series of average island structures. In Fig. 3.2 (page 33), these site densities were summarized in either the {100} or {111} direction. To do this, the densities of corner sites and {112}-related sites were equally split over these two classes. Figure C.6 shows the correlations between the charge of the A_{2-4} peaks and the corresponding surface sites as discussed in Chapter 3. Despite the value of the correlation coefficient, there is a clear discrepancy in the correlation in Fig. C.6A, which originates from the fast increase of the A_2 peak during the first three cycles (see Fig. 3.2 on page 33). The underlying reasons for this behavior could be the formation of vacancy edge sites with a {110} geometry. Another explanation could be that some of these step sites were already present at the initial surface and get ‘cleaned’ during the ORCs. Neglecting the data of the first three cycles to determine the correlation coefficient, we obtain a correlation coefficient of 0.93. The grey line in Fig. C.6 shows the correlation between the {110} facet sites and the A_4 charge after applying a moving average (with a width of 5 datapoints) filter to the site densitities. This leads to a significantly larger correlation coefficient (0.93 vs. 0.54.). The large variation in the facet site densitities is considered to be a fitting artefact, as the absolute densities of these sites are rather low.

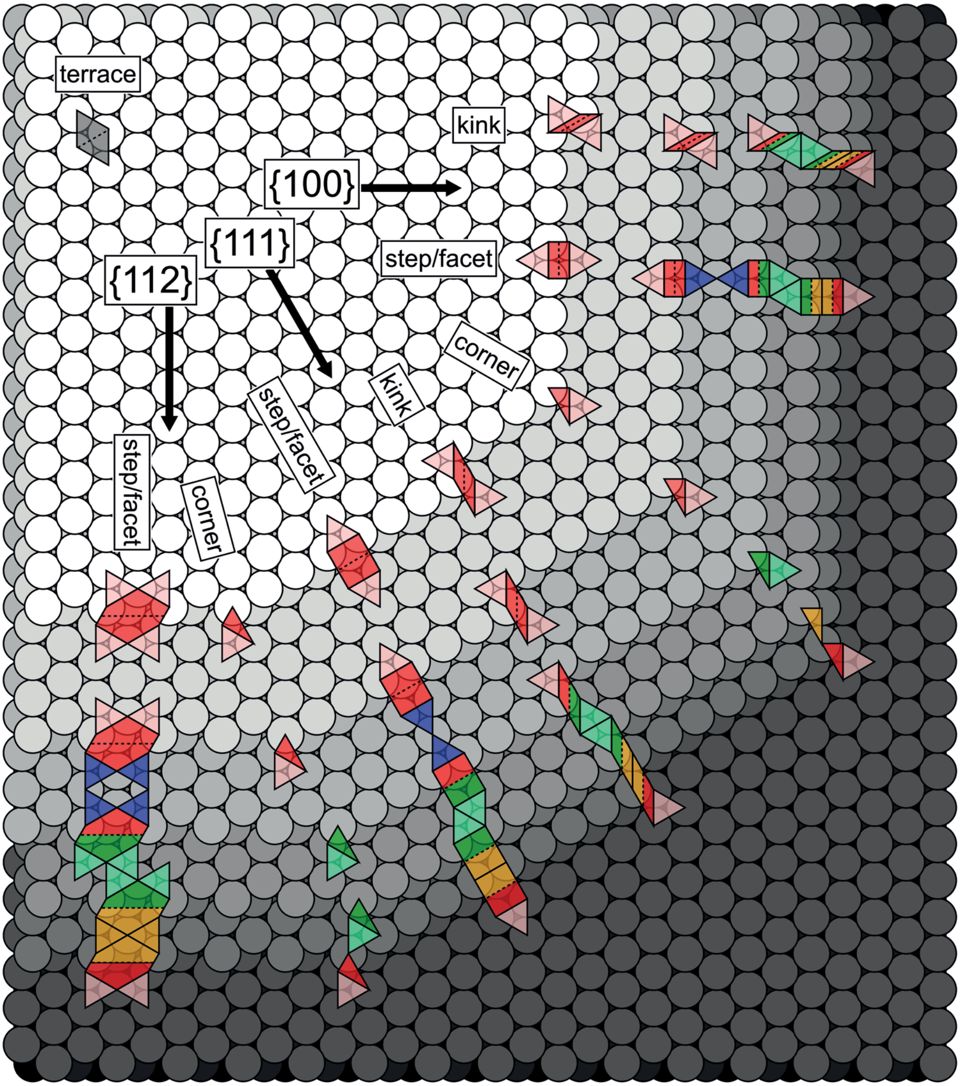

Fig. C.4 | Site assignment: Assignment of the different parts of the unit cells to 'separated defects', 'wide facets', 'narrow facets', and 'low index facets' (red, blue, green, and yellow, respectively) Note that for 'wide facets' only the terrace sites are expected to show different behavior, the step itself is considered a 'separated defect'. Terrace sites belonging to 'separated defects' and 'narrow facets' are indicated in light red and light green, respectively. The geometry of 'wide facet' kink sites is explained in the text, but not shown here.

Table C.1 | Site assignment: Overview of all different surface geometries that were considered in the counting process. ‘T’ indicates terrace sites, belonging to a specific ‘defect’ geometry as indicated by its subscript label.

Direction/Type		‘Separated defect’	‘Wide facet’	‘Narrow facet’	‘Low index facet’
{100}	‘Defect’	{100} step	{100} step	{311} facet	{100} facet
		{100} kink	{100} kink	{311} kink	{100} kink facet
	Terrace	$T_{\{100\}-step}$	{211} facet	{311} facet	-
		$T_{\{100\}-kink}$	{211} kink	{311} kink	-
{111}	‘Defect’	{110} step	{110} step	{331} facet	{110} facet
		{110} kink	{110} kink	{331} kink	{110} kink facet
	Terrace	$T_{\{110\}-step}$	{221} facet	{331} facet	-
		$T_{\{110\}-kink}$	{221} kink	{331} kink	-
{112}	‘Defect’	{112} step	{112} step	{321} facet	{531} facet
	Terrace	$T_{\{112\}-step}$	{753} facet	{321} facet	{531} facet
$\text{Corner}_{\{100\}-\{111\}}$	‘Defect’	Corner	Corner	Narrow Corner	LI Corner
	Terrace	T_{corner}	T_{corner}	Narrow Corner	-
$\text{Corner}_{\{111\}-\{112\}}$	‘Defect’	Corner	Corner	Narrow Corner	Narrow Corner
	Terrace	T_{corner}	T_{corner}	Narrow Corner	Narrow Corner

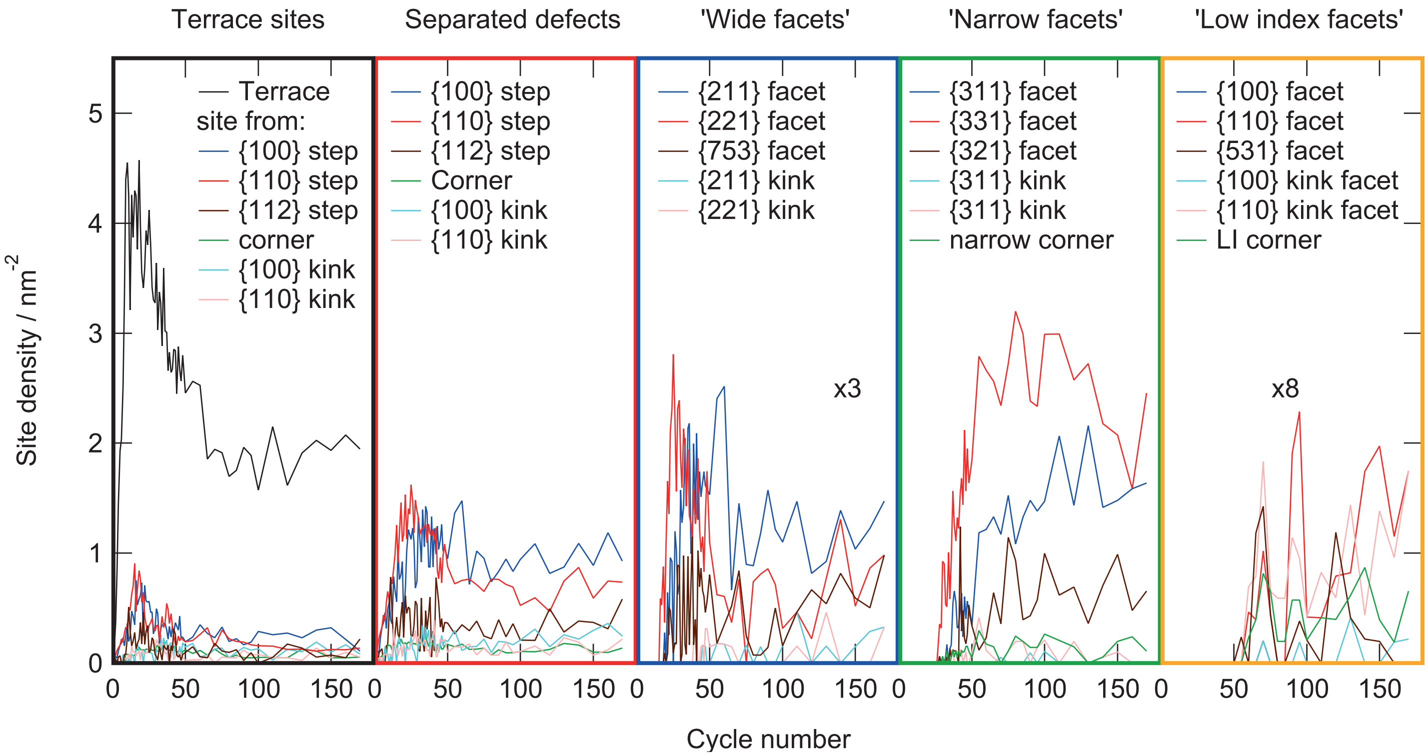

Fig. C.5 | Individual site densities: The evolution of the site densities for all different surface geometries considered.

Table C.2 | Counting example: Site counts of the colored sites in Fig. C.4 after normalization.

Type	Normalized site counts
{100} step/facet	3 {100}-steps; 2 $T_{\{100\}-step}$; 1 {211} facet; 2 {311} facets; 1 {100} facet
{111} step/facet	3 {110}-steps; 2 $T_{\{110\}-step}$; 1 {221} facet; 2 {331} facets; 1 {110} facet
{112} step/facet	6 {112}-steps; 4 $T_{\{112\}-step}$; 2 {753} facets; 4 {321} facets; 2 {531} facets
{100} kink	3 {100}-kinks; 3 $T_{\{100\}-kink}$; 2 {311} kink facet; 1 {100} kink facet
{111} kink	3 {110}-kinks; 3 $T_{\{110\}-kink}$; 2 {331} kink facet; 1 {110} kink facet
$\text{Corner}_{\{100\}-\{111\}}$	1.5 Corner; 1.5 T_{corner}; 1 Narrow corner; 0.5 LI corner
$\text{Corner}_{\{111\}-\{112\}}$	1.5 Corner; 1.5 T_{corner}; 2 Narrow corners

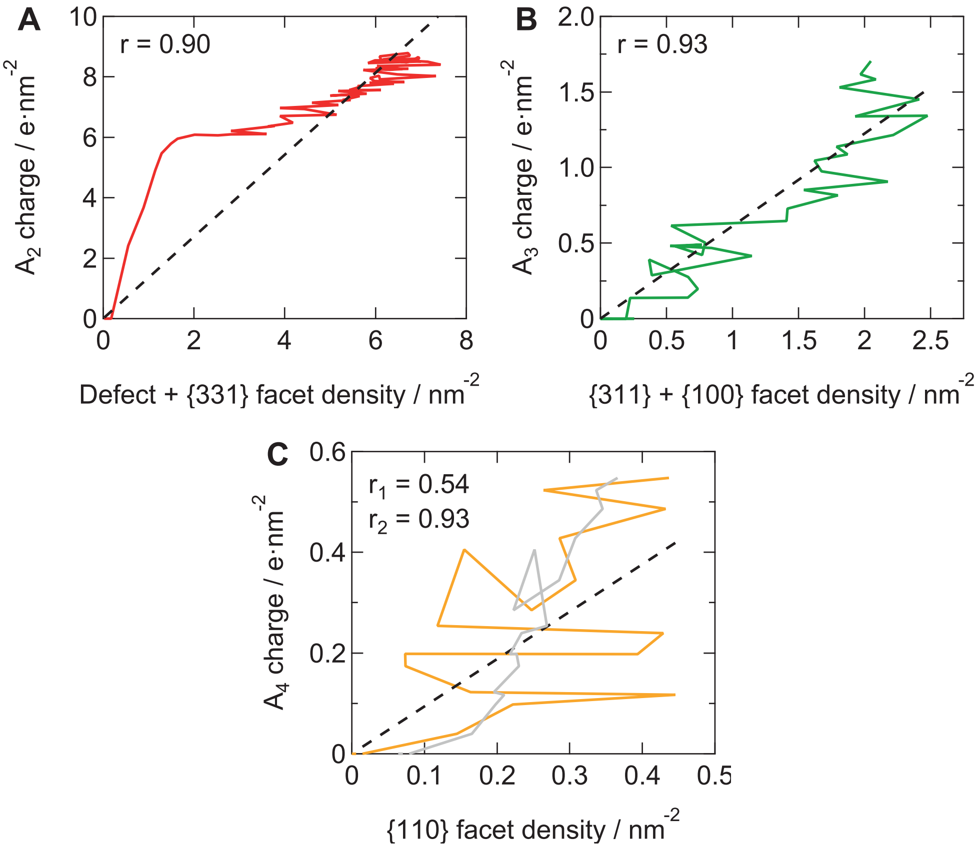

Fig. C.6 | Correlations between peak charge and site densities: **(A)** A_2 charge vs the density of 'separated defects' + {331} facets. **(B)** A_3 charge vs the density of {311} + {100} facet sites. **(C)** A_4 charge vs the density of {110} facet sites. A detailed motivation behind these correlations is provided in Chapter 3.

C.4 CV fits

Methods to determine the different contributions to the hydrogen region of Pt CVs have been discussed in literature before. Here, we use the approach described by McCrum and Janik, who fit an inverse hyperbolic cosine to the broad terrace feature and gaussian functions to the 'defect'-peaks.[4] To capture the changing shape of the A_2-peak, it turns out that this peak needs requires fitting with a summation of two gaussians centered around the same potential. To obtain good fits and limit the degrees of freedom, the (111) terrace feature is fixed for all CVs. An example of the fitting result (after 150 cycles) is shown in Fig. C.7.

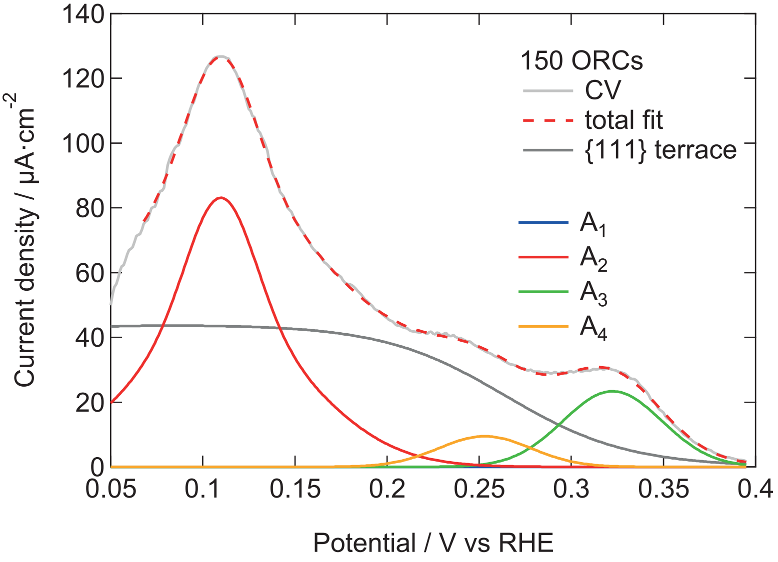

Fig. C.7 | CV fitting: Example of the charge determination for the different contributions to the hydrogen desorption reaction.

References

1. Nečas, D. & Klapetek, P. Gwyddion: an open-source software for SPM data analysis. *Cent. Eur. J. Phys.* **10,** 181–188 (1 2012).
2. Villarrubia, J. Algorithms for scanned probe microscope image simulation, surface reconstruction, and tip estimation. *J. Res. Natl. Inst. Stand. Technol.* **102,** 425 (1997).
3. Soille, P. *Morphological Image Analysis* 392. eprint: `1011.1669` (Springer Berlin Heidelberg, 2004).
4. McCrum, I. T. & Janik, M. J. Deconvoluting Cyclic Voltammograms To Accurately Calculate Pt Electrochemically Active Surface Area. *J. Phys. Chem. C* **121,** 6237–6245 (2017).

D

Platinum nanoisland structures

This appendix contains the series of nanoisland structures, belonging to Chapter 3. The data are directly accessible via the digital version of this thesis using an appropriate pdf viewer (e.g. Acrobat Reader). Other movies, containing results described in Chapters 2-4 can be accessed via the supplementary information of the corresponding publications.